Case Studies in Thermal Engineering 27 (2021) 101234

Contents lists available at ScienceDirect

Case Studies in Thermal Engineering

journal homepage: www.elsevier.com/locate/csite

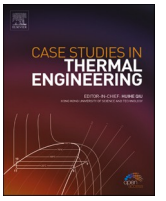

Pixel frequency based railroad surface flaw detection using active infrared thermography for Structural Health Monitoring

Bilawal Ramzan [a], Muhammad Sohail Malik [a,*], Milena Martarelli [b], Hafiz T. Ali [c], Mohammad Yusuf [d], S.M. Ahmad [a]

[a] Faculty of Mechanical Engineering, GIK Institute of Engineering Sciences and Technology, Topi, 23460, Pakistan
[b] Department of Mechanical Engineering, Università Politecnica delle Marche, Via Brecce Bianche, 60131, Ancona, Italy
[c] Department of Mechanical Engineering, College of Engineering, Taif University, P.O. Box 11099, Taif, 21944, Saudi Arabia
[d] Department of Clinical Pharmacy, College of Pharmacy, Taif University, P.O. Box 11099, Taif, 21944, Saudi Arabia

ARTICLE INFO

Keywords:
Thermography
Railroads
Infrared radiation
Surface flaws
Non-destructive testing
Structural health and monitoring

ABSTRACT

With rapid increase in operation and development of high-speed trains, inspection of railroad surface flaws has become an important aspect for safe and reliable operation of rail network. Non-destructive testing using active infrared thermography has been useful in determining the structural health of different structures with additional benefit of robustness in overall inspection system. This study is based on detection of artificial surface flaws on an in-service railroad. Transverse and longitudinal flaws of various dimensions were machined on rough and smooth rail surface. The railroad surface was thermally stimulated to a temperature equivalent to practical conditions. Emitted radiations from rail surface were captured by an infrared camera to detect cracks. Results show a comparison between the surface flaws on rough and smooth rail surface. Subsequently, raw infrared images were post-processed by statistical image improvement to quantitatively analyse the results. Significant change in the frequency distribution of pixel intensity is observed as the flaw size and depth changes giving a clear quantification of crack topology. A comprehensive and inexpensive solution for damage diagnosis will be offered to railway authorities for Structural Health Monitoring (SHM) and NDT by the proposed framework.

1. Introduction

Most of the rail defects that lead to serious rail accidents occur at the rail head due to rail wheel contact [1]. Fatigue loading generated by rail-wheel contact plastically deforms rail head steel and surface flaws of different orientation and dimension begin to appear. Production defects (line), local battering, flaking, local grooving and engine or wheel burns are various types of flaws developed at rail head. Creep forces are induced due to localized rolling action at rail/wheel contact patch. These are longitudinally oriented forces which are created by wheel traction on the rail or by compensating for different wheel diameters impacting the rail as a result of a sharp curve [2]. The list of steps for the diagnostics of surface flaws on an in-service railroad is provided in Fig. 1. Component of creep forces is also generated in transverse direction due wheelset lateral orientation on rail surface. Owing to continuous slippage of wheels on the rail track, it also causes wheel burning on the rail. The creep effect is shown in Fig. 2 [2].

Apart from creep forces; rolling contact pressure, shear and bending forces are also produced as a result of vehicle weight on rail

* Corresponding author.
E-mail address: sohailmalik@giki.edu.pk (M.S. Malik).

https://doi.org/10.1016/j.csite.2021.101234
Received 11 February 2021; Received in revised form 5 July 2021; Accepted 8 July 2021
Available online 10 July 2021

head. Constricted elongation of welded rails along with residual stresses from manufacturing and in-field welding generates thermal stresses. Stress distribution [3] in rail has been shown in Fig. 3. Dynamic loading has always been a challenge while designing railway bridges. The vibration of the railway reinforced system will be influenced by the dynamic load of passing trains at a speed of 200 km/h or above; resonance phenomenon may be induced if the frequency of the dynamic load and the railway reinforced system are close to each other; the amplitude of the reinforced system will be greatly increased. During the passage of wheelset on rail road due to the

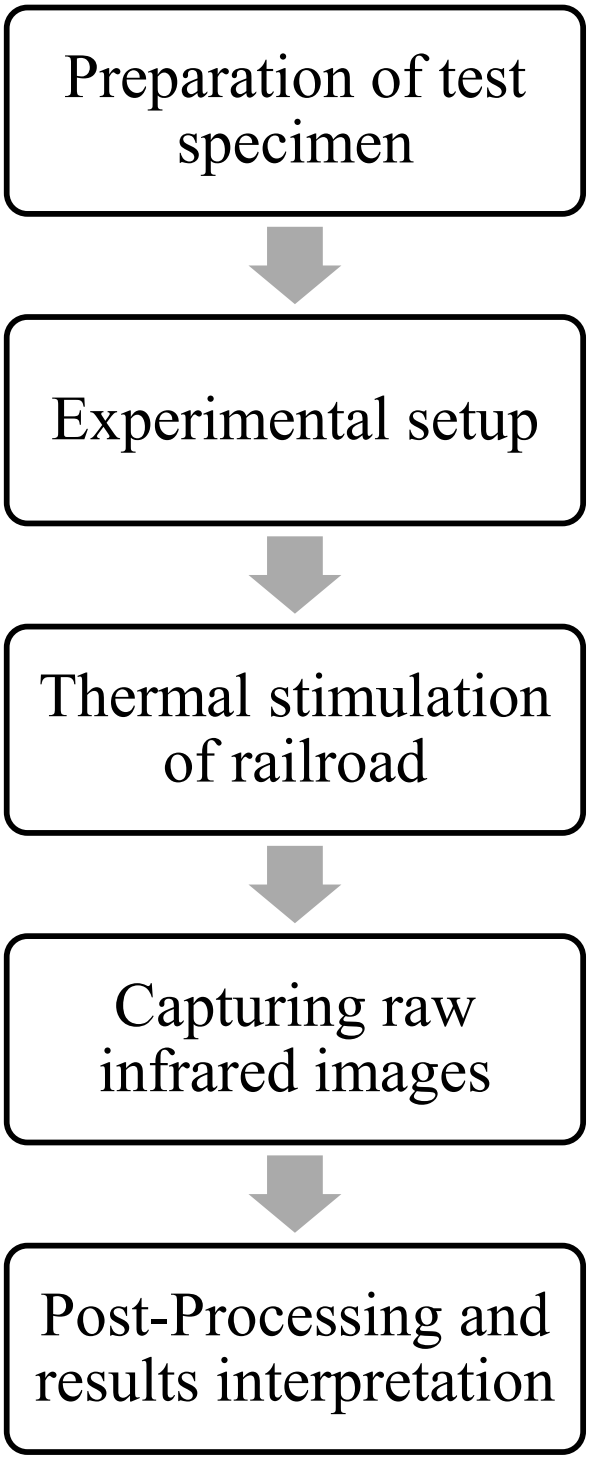

Fig. 1. Sequence of operations for characterization of railroad surface flaws.

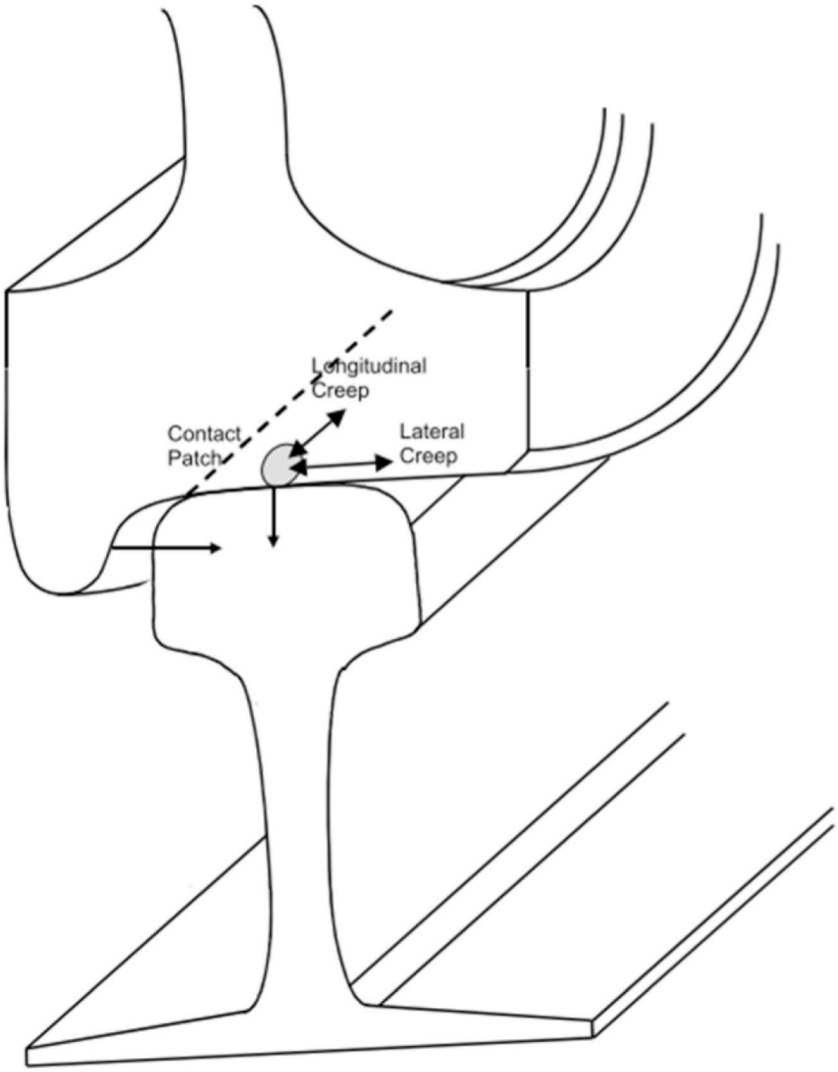

Fig. 2. Creep forces along lateral and longitudinal direction rail surface.

effect of transverse force and vibration the load exerted by one or more wheels may decrease and such large imbalance of wheel load can cause derailment. The irregular movements of locomotive and inertia of moving parts induce dynamic effects generated during train motion which enhances rolling load which results in irregular resistance or defects on rail track [4].

Dr. Elemer Spery started the inspection of railway cracks, for the first time, in USA back in 1920 [5]. Since then, substantial R&D has been carried out to determine cause and early detection of rolling contact fatigue (RCF) cracks and stress concentration cracks (SCC). Several non-destructive testing methods (NDTs) for defect detection have been used for this purpose [6]. Eddy current or visual inspection, magnetic flux leakage testing (MFL), ultrasonic testing and magnetic particle inspection are frequently used NDT methods for railroad inspection [7]. To obtain robustness in inspection process; several new NDT equipment have been introduced including Electromagnetic Acoustic Transducers (EMATs) [8–11], high speed cameras [12], field gradient imaging (FGI) [13], multi frequency eddy current sensors, laser ultrasonic [14–16] infrared thermography and acoustic sensors [17]. The reliability of inspection methods for flaw detection using high-energy laser or ultrasonic pulses was determined by the probability of detection (POD) principle and POD curves were implemented to validate the authenticity of inspection methods [18,19].

Nevertheless, characterization of rail head flaws is difficult because of their clustered distributions and geometric interactions. Infrared thermography (IRT) gains attention with the advantage of non-contact sensing and simple visualization of minor thermal variations compared to the aforementioned NDT techniques [20–26]. Owing to its operational capabilities in terms of robust inspection, remote/real-time operation, high temperature precision, 2D-contour thermal image representation, high SNR and radiation emission within safe limits, use of active IRT has been increased significantly in NDT [27–30]. Due to its advantages, IRT has emerged as a promising technique for NDT. Based on the inductive transient thermal sequences for automatic NDT, Gao [31] extracted spatial and time patterns. Wilson [32] utilized pulsed eddy current thermography to detect various cracks generated due to RCF. In IRT

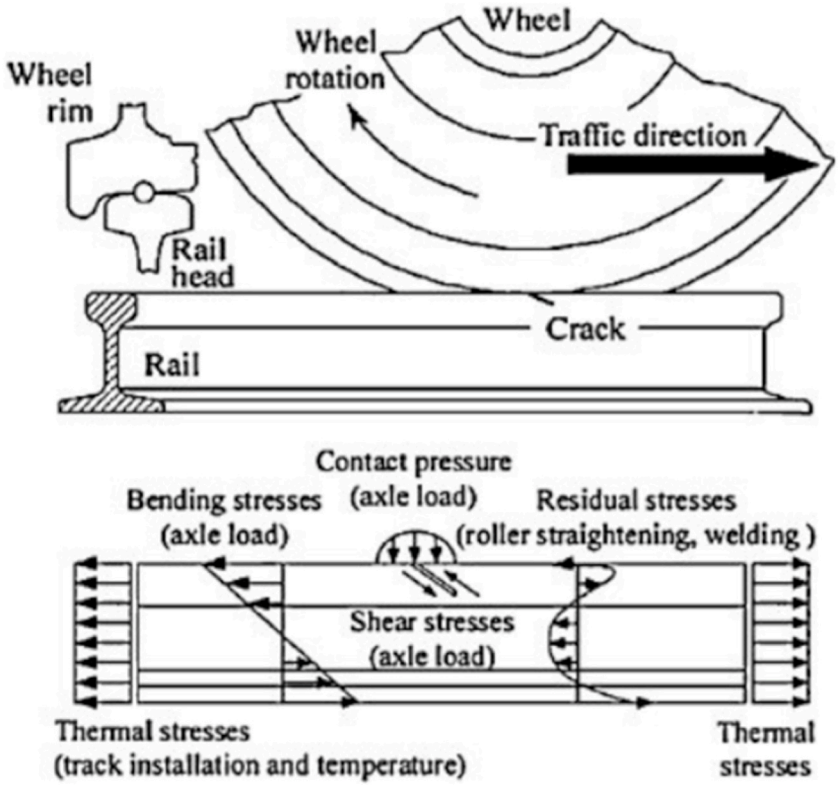

Fig. 3. Applied load components during the passage of vehicle on continuously welded rail.

reflective mode, however, the problems with limited heating area, non-homogeneous heating and coil blocking effect still effect the quantitative characterization accuracy of defects. Jäckel [33] enhanced the crack detection contrast by induction thermography and proposed electromagnet yokes to apply external magnetic field. Lahiri [34] recorded a wide area of low frequency alternating magnetic

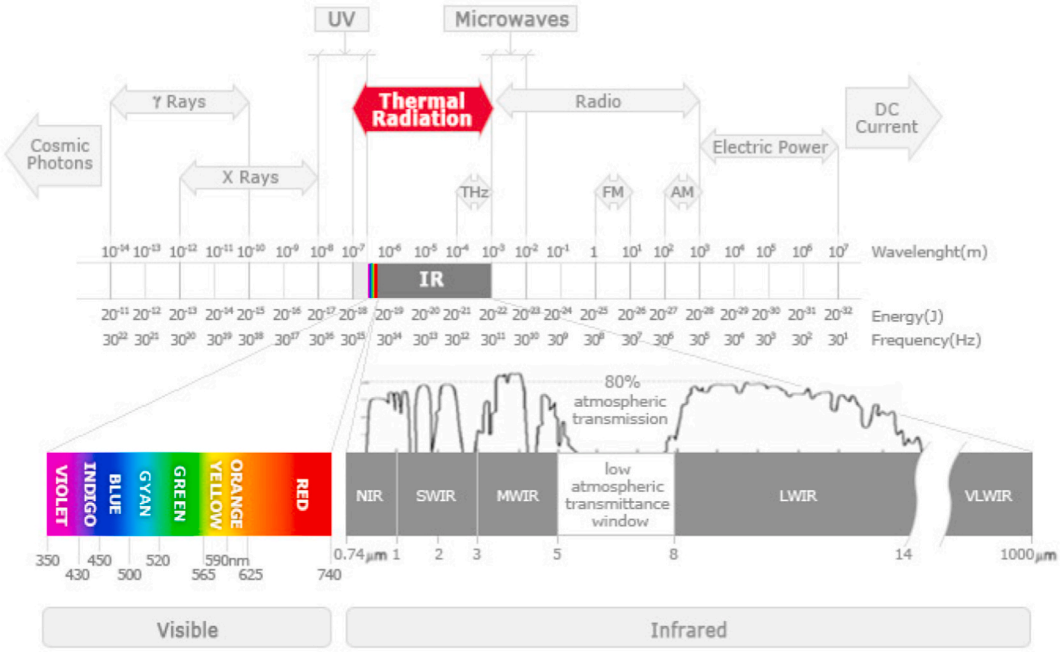

Fig. 4. Electromagnetic spectrum showing LWIR energy band.

field for evaluating defects through thermographic NDT. A measuring system with induction generator scanning was developed by Netzelman [35] for the inspection of rail surface defects at different speeds of up to 15 km/h. Shepard [36] demonstrated improvement and the analysis of pulsed thermographic data with enhanced spatial and temporal accuracy for defect detection.

A review of previous studies on active IRT show the limitation in detecting variety rail head surface flaws. The focus of this work is, therefore, on detecting both longitudinal and transverse surface cracks on rough and smooth surface, as conventional inspection systems are time consuming and not practical with development of high-speed trains. And to propose an effective, efficient and robust inspection system, with minimum maintenance. All these features are the requirement of a modern rail inspection system.

2. Principle of infrared thermography

Electromagnetic radiations are emitted from all bodies that are above absolute zero temperature (−273.15 °C). The quantity of emitted from the surface of an object is related to its thermal efficiency, called emissivity and its temperature. Radiations emitted throughout the electromagnetic spectrum are in the form of energy particles known as photons. From the complete electromagnetic spectrum only Thermal Infrared (TIR) or Long-Wavelength Infrared (LWIR) energy band is studied IRT via a sensor that is capable of sensing wavelength (7 μm–14 μm) and frequency (2.1×10^{13} Hz to 4.3×10^{13}) interval [37]. LWIR energy band is shown in Fig. 4 below [38]. The infrared radiation in this band of energy spectrum is referred to as thermal radiation, and the band is selected because of the relationship between an object's temperature value and the quantity of radiation emitted over the temperature spectrum from −73 °C to 125 °C is maximum [39].

Thermal radiations emitted from an object surface are measured by thermal sensor which formulates sensor matrix incorporating a thermographic camera. IRT utilizes Stefan-Boltzmann relation to determine the value of body's surface temperature [40].

$$E = \varepsilon \sigma T^4 \tag{2.1}$$

where E represents emitted thermal radiation per unit area (W/m^2); T denotes absolute surface temperature of the object; ε is the emissivity of object's surface and σ denotes Stefan Boltzmann constant whose value is 5.67×10^{-8} $W/(m^2K^4)$.

Although there are several factors that can effect the accuracy of thermographic inspection. Environmental factors such as reflection and radiation of thermal waves in environment can disturb the acquisition and processing of thermal data. the effect of environmental aspects consists of: reflection and radiation of thermal waves, the condition of the material and impact surrounding convention on signal recognition. The temperature difference will always ensure the accuracy of the results amongst temperature of the surface of specimen and the thermal gradient that the infrared records. Usually, the temperature gradient between non-defective and defection regions is minimum [41,42]. The infrared radiation energy E that the infrared thermal camera senses consist of three parts as given by equation (2.2)

$$E = \varepsilon \sigma T^4 + E_a + E_{atm} \tag{2.2}$$

Where E_a is the radiation reflected from surrounding to specimen; E_{atm} denotes atmospheric radiation received by IR camera sensor. The thermal image will be influenced by errors affecting the accuracy of the detection if the sum of E_a and E_{atm} are not identical at each pixel, regardless of the uniformity of emissivity and temperature at each point on the material.

2.1. Governing equations

Heat flow through the specimen is governed by equation (2) given below [43]:

$$-\left(\frac{\partial q_x}{\partial x} + \frac{\partial q_y}{\partial y} + \frac{\partial q_z}{\partial z}\right) + Q = \rho c \frac{\partial T}{\partial t} \tag{2.3}$$

In equation (2), components of heat flow per unit area in are denoted by q_x, q_y and q_z; specific heat capacity of the specimen is represented by c; duration of heat flow is denoted by t; T is the temperature of object's surface; specimen density is denoted by ρ and internal heat generation per unit volume is denoted by Q.

Components of heat flux can also be written in terms of Fourier's Law [44].

$$q_x = -k\frac{\partial T}{\partial x},\ q_y = -k\frac{\partial T}{\partial y},\ q_y = -k\frac{\partial T}{\partial z} \tag{2.4}$$

In equation (3), k represents the co-efficient of thermal conductivity. By using Fourier's law, equation (2) can also be written as:

$$\left[\frac{\partial}{\partial x}\left(k\frac{\partial T}{\partial x}\right) + \frac{\partial}{\partial y}\left(k\frac{\partial T}{\partial y}\right) + \frac{\partial}{\partial z}\left(k\frac{\partial T}{\partial z}\right)\right] + Q = \rho c \frac{\partial T}{\partial t} \tag{2.5}$$

The unique solution for underlaying physical problem can be obtained by utilizing following boundary conditions (BCs):

$$\text{SpecifiedHeatflow} \quad q_{s=} q_x e_x + q_y e_y + q_z e_z \tag{2.6}$$

$$\text{ConvectionBC} \quad h(T_s - T_e) = q_x e_x + q_y e_y + q_z e_z \tag{2.7}$$

$$\text{SpecifiedTemperature} \quad T_s = T(x, y, z, t) \tag{2.8}$$

$$\text{RadiationBC} \quad \varepsilon\sigma T^4 - \alpha q_{rad} = q_x e_x + q_y e_y + q_z e_z \tag{2.9}$$

where e_x, e_y, and e_z represent the direction cosine of outward normal to the surface; co-efficient of surface absorption is denoted by α; surface temperature of the specimen is denoted by T_s; convection heat transfer co-efficient is represented by h and radiation heat transfer component per unit area is represented by q_{rad}.

Notice that only surface temperature of the specimen can be measured via IRT. Hence, any surface anomaly or imperfection can be detected by IRT if the specimen is thermally stimulated by some artificial heat source during analysis (active thermography) [45]. Otherwise, surface flaws cannot be detected with captured thermal images.

3. Methodology

3.1. Specimen

A standard 30 lb flat bottom T-section rail specimen was selected to for the inspection of surface flaws. The length of rail track is larger as compared to its thickness and width. As defined by American Society of Civil Engineers (ASCE), the dimensions of rail section [46] are descripted in Fig. 5 below:

The specimen is composed of 880-grade steel rail sheets. The ultimate tensile strength (UTS) of the sample is 880 MPa which implies the internal resistance of the material to the external load. If the applied load exceeds beyond UTS permanent failure of specimen will occur [47].

Mechanical and chemical properties of rail sample are provided in Table 1 and Table 2 respectively:

3.2. Artificial flaws

Rail specimen used for studying artificial flaws is shown in Fig. 6. Rectangular slots were machined to simulate surface flaws due to RCF and creep forces. These cracks were generated at a particular distance on the railway surface [2,49]. To characterize rail head surface flaws of various features i.e., flaw type, surface finish and crack orientation, specimen surface was divided into four segments. Two types of artificial flaws were machined on smooth and rough segments of rail specimen. Four transverse slots were machined across the surface of the rail head for the first set and four longitudinal slots were machined across both surfaces for the second set. The depth of the slots ranges from 0.5 mm to 2 mm, while the length of the longitudinal slots ranges from 20 to 30 mm, giving us a total of 12 slots of varying sizes and orientations across the rail surface. The defect width (slot opening) of 1 mm was kept constant throughout the artificial cracks. Table 3 provides geometric parameters of these defects with respect to surface type. Fig. 6 show longitudinal and transverse flaws on rough and smooth surface. LF1R-LF4R, LF1S-LF4S, TF1R-TF4R and TF1S-TF4S represent transverse and longitudinal flaws on both surfaces respectively [50]. The characteristics of various segments of rail specimen are given in Table 3 below:

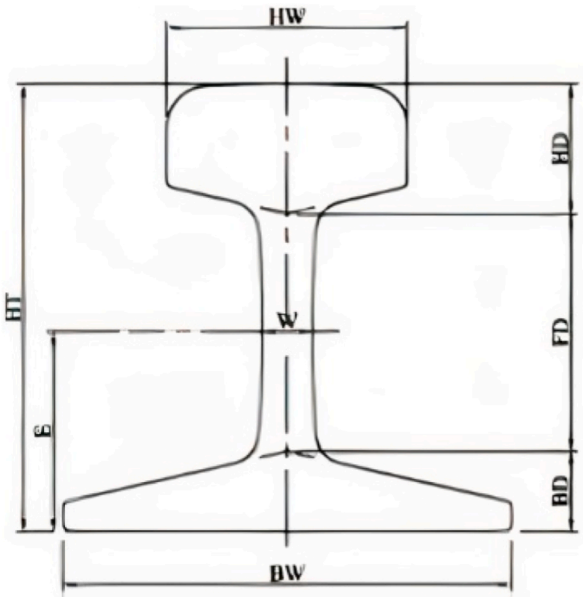

Fig. 5. Dimensions of 30 lb ASCE rail section. Length L = 3.66 m Width w = 0.7 cm HW = 4 cm HD = 2.5 cm E = 3.75 cm FD = 4 cm BD = 1.5 cm BW = 7.5 cm HT = 7.5 cm.

Table 1
Mechanical properties of rail specimen as per IRS specifications [48].

Mechanical properties	Value	Unit
Ultimate tensile strength	≥880	MPa
Percentage elongation	10%	–
BHN hardness	≥260	–

Table 2
Chemical properties of rail specimen as per IRS specifications [48].

Chemical Composition	Weight percentage (% by mass)
Carbon	0.6–0.8
Manganese	0.8–1.13
Silicon	0.19–0.5
Sulphur	<0.035
Phosphorus	<0.035

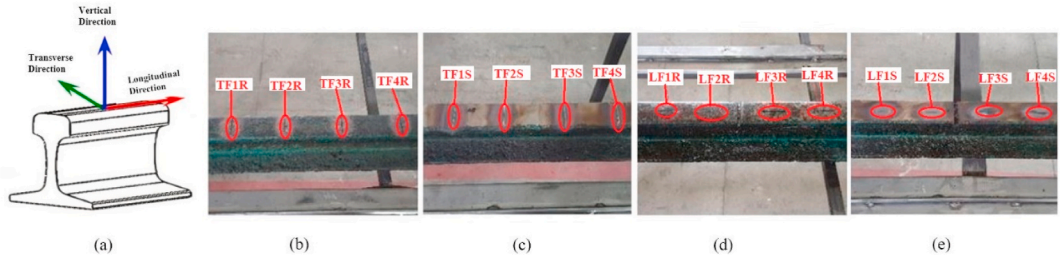

Fig. 6. Orientation of artificial surface flaws on rail specimen (a) Section of rail track used studying artificial flaws (b)Transverse Flaws on rough surface form TF1R to TF4R (c) Transverse flaws on smooth surface from TF1S to TF4S (d) Longitudinal flaws on rough surface from LF1R to LF4R (e) Longitudinal flaws on smooth surface from LF1S to LF4S.

i. Since we are using an in-service rail specimen which has surface roughness due wear and rust. Therefore, first portion of the sample was kept as it is. The effects of corrosion and surface roughness on thermographic data in the vicinity of surface flaws are studied in this segment.
ii. The surface of rail specimen was grinded to produce a polish surface for second part of the sample. Surface finish being the difference between first and second segments of specimen.
iii. The third part of the sample is developed by the forming of surface cracks. These flaws are laterally oriented across rail head surface.
iv. Fourth and third section of the specimen are differed in term of crack orientation. For this segment, cracks are oriented longitudinally along the length of rail specimen.

3.3. Surface flaw characterization by IRT

Active infrared thermography was used to characterize surface defects by applying a uniform heat flux on the rail surface for a specific time period and measuring the distribution of temperature through the heated region by an infrared camera. Surface flaws appear in thermograms as local cold or hot regions on a 2D-contour plot, as the defects disrupt the heat flow applied to the surface. In the recorded infrared thermal images, defects are thus detected through the monitoring of these inhomogeneous temperature regions. All the experiments were performed as per ANSI/ASTM E1213 standards to record the minimum temperature variation in order to distinguish between defective and non-defective regions. Also, the equipment used in the experiment is according to the specification descripted in ANSI/ASTM CP-189 [51].

The underlying physical phenomena which results in the thermal signature of flaws should be pointed out. To comprehend the mechanism of IRT; we use Fourier's Law by using equation (3), it can be re-written as:

$$\boldsymbol{q} = -k\left(\boldsymbol{i}\frac{\partial T}{\partial x}+\boldsymbol{j}\frac{\partial T}{\partial y}+\boldsymbol{k}\frac{\partial T}{\partial z}\right) = -k\nabla \boldsymbol{T} = \frac{1}{\boldsymbol{R_t}}\nabla \boldsymbol{T} \tag{3.1}$$

Table 3
Geometric parameters for artificial flaws. Crack opening (width) for all the cracks is kept constant at 1 mm.

Parameters	Nomenclature																
	TF_{1R}	TF_{2R}	TF_{3R}	TF_{4R}	TF_{1S}	TF_{2S}	TF_{3S}	TF_{4S}	LF_{1R}	LF_{2R}	LF_{3R}	LF_{4R}	LF_{1S}	LF_{2S}	LF_{3S}	LF_{4S}	Unit
Flaw orientation	Transverse								Longitudinal								
Crack length	40	40	40	40	40	40	40	40	20	25	30	35	20	25	30	35	mm
Crack depth	0.5	1	1.5	2	0.5	1	1.5	2	0.5	1	1.5	2	0.5	1	1.5	2	mm

In equation (9), applied heat flux on rail surface is denoted **q**; thermal resistivity is represented by $\mathbf{R_t}$ and temperature gradient is represented by $\nabla\mathbf{T}$. When a heat flux is applied a surface in the vicinity of an anomaly, a higher temperature gradient or temperature distribution step occurs because of variation in localized thermal resistivity $\mathbf{R_t}$ due to which surface imperfections or defects are inspected. In the case of three-dimensional heat conduction for in-service railway track inspection with a localized heat source, **q** is not constant and $\mathbf{R_t}$ is also affected. But the qualitative study of railhead surface cracks from thermal images is still feasible. As a result, higher R_t results in a reduced cooling rate and thus a higher maximum temperature when the heat is applied in the vicinity of a crack as compared to a non-defective surface, eventually resulting in crack signatures on thermogram. Experimental setup as well as schematic configuration for IRT inspection system is shown in Fig. 7.

As shown in Fig. 7, experimental setup for inspection system consists of a thermally stimulated rail specimen, platform for mounting rail track and an IR camera for capturing raw IR images. Flir TG165 infrared camera was used to record thermograms after application of thermal stimulus by 1000 W heating torch. Surface of rail specimen was thermally stimulated 20 °C above ambient temperature to match the practical conditions by manually moving and restraining torch at a distance of 10 cm from railhead. The heat was applied in short pulses of 2–5 s. This form of thermal stimulation to detect surface flaws is referred as short pulse. After application of surface heat flux for a specific time interval; cooling rates for both sounded and defective surface are recorded. The selection of emissivity is another critical parameter for rail track thermography. Emissivity is the property of an object which, in contrast to the black body, indicates the radiation emitted by the surface at a given temperature. The sum of resistivity and emissivity for an opaque object is unity. Highly emissive materials thus have low reflection and infrared inspection is convenient whereas noise in thermal images is induced by high reflection. The sample was vulnerable to temperature variation during the capture of infrared images because the examination was carried out in an open area. As certain thermal radiations are often dispersed in the surrounding region which cause an inherent noise in recoded raw thermal images, so post-processing is necessary to distinguish defects and irregularities from the non-defective surface. In order to achieve a better signal to noise ratio) SNR, a statistical moment approach has been utilized for quantitative analysis of temperature distribution across the surface [52].

4. Results and discussion

4.1. Longitudinal flaws

Fig. 8 provides a comparison between thermal signatures for longitudinal flaws on smooth and rough surface. The dimensions of these flaws are provided in Table 3. To check the feasibility of inspection method for in-service rail track exposed to harsh environmental conditions thermographic behaviour on both types of surfaces was observed. Thermal stimulation was applied to surface containing flaws and thermal images were captured to observe the thermal contrast between non-defective and defective surface. The principle of crack inspection is based on the principle of varying cooling rates between sounded and defective region. Due to this phenomenon the characterization of surface flaws was made by observing the thermal intensity of pixel across the surface. The darker pixels on thermogram represent the cooler region whereas brighter pixels denote hotter regions. Fig. 8 below shows the thermogram as well as the frequency of surface temperature distribution on a defective surface. As it can be seen that in the absence of any surface defect the variation in temperature distribution across the surface is minimal.

Temperature histogram in Fig. 8 (b) depicts that surface of specimen is at 54 °C with negligible temperature variations. While a significant thermal contrast can be observed in Fig. 9 and Fig. 10 respectively due to the presence of surface flaws which cause inhomogeneous temperature region on the thermograms.

In the event of any surface imperfection a thermal contrast occurs between non-defective and defective surface. Pixel intensity in defective region will differ from rest of surface. Though the detection principle for flaws on smooth and rough surface is same but the

interpretation can be different. In side by side comparison between thermograms for both surface it is quite obvious that pixel intensity is different. The smooth metallic surface give rise to surface reflection that may result in misinterpretation of surface temperature. On the other hand, for rough surface, due to presence of oxides and rust layer absorption of radiation increases which appear as brighter region. Therefore, evaluation of crack from raw infrared image is not sufficient to quantitatively determine the defective region on specimen.

To compensate for this unwanted noise pixel intensity was measured in spot region of 10 mm in diameter at a stand-off distance of 203 mm which is prescribed stand-off distance for accurate temperature measurement by Flir TG165 infrared camera. The maximum temperature limit for thermal image post-processing was selected by measuring the maximum pixel intensity at region of interest and extrapolating the maximum temperature for each thermogram with reference to pixel intensity and measured temperature of infrared camera. The frequency distribution histogram for all four longitudinal cracks on rough and smooth surface provide quantitative characterization of surface flaws. The heat flow across the surface has been interrupted by the presence of surface anomaly causing reduction in cooling rate in the vicinity of defect, this effect appears as thermal contrast in thermographic data. Detection of cracks on rough surface in Fig. 8 (a), (c), (e) and (g) is more pronounced due better absorption of thermal radiations. A visually enhanced thermal contrast is present between sound and defective surface. As the crack depth increases; cooling rates varies for deeper cracks that take longer to reach the surface temperature which is depicted in Fig. 8 (e) and (g). The thermal contrast between sound and defective region in terms of surface temperature has been shown quantitatively in thermal image histograms. The variation in frequency of surface temperature is the reason behind visualization of thermal contrast for detection of crack on rail surface. The comparison between thermograms for crack detection on rough and smooth surface suggests that even after post processing the detection of flaws on smooth surface is challenging. This is primarily due to increase reflection from the smooth surface the thermal contrast is not as much distinct as in case of rough surface flaws. Fig. 8 (b), (d), (f) and (h) provide thermograms as well as quantitative representation of thermal contrast in the form temperature frequency histogram. Thermal intensity is, therefore, increased to extract the meaningful information which reduces environmental noise and other factors affecting flaw inspection. All the histograms for cracks on rough surface are left skewed tailing more temperature data on left side of the peak providing a thermal contrast. While for cracks on smooth surface the temperature distribution histogram approaches a traditional bell curve giving us a uniformly varying thermal contrast.

To quantitively assess the thermal contrast for each type on both surface SNR has been calculated. There are many descriptions for estimation of SNR in previous literature. SNR for surface flaw has been calculated by using equation (10),

$$SNR = 10\log_{10}\left(\frac{abs(\mu_s - \mu_N}{\sigma}\right) \quad 4.1$$

In above equation, μ_S is the arithmetic mean of pixels in defective region; μ_N is the arithmetic mean of pixels in sound region and σ is standard deviation of pixels in non-defection region which is typically characterized as background noise [53]. The SNR for LF1S to LF4S lies between 33 and 36 dB while for LF1R to LF4R the range of SNR is 30–34 dB which slightly less than the later due unwanted debris and corrosion on rough surface that resulted in reduce signal relative to smooth section. But the quantitative inception of surface flaws in both cases has been made because overall range for SNR is sufficiently higher.

4.2. Transverse flaws

Fig. 9 shows the quantitative evaluation and comparison for transverse flaws on smooth and rough rail surface. The dimensional parameters of these flaws are given in Table 3. The variation in depth for these flaws is same as in case on longitudinal flaws. As it can be seen in the temperature frequency histogram below; sample surface temperature distribution form has been changed by shallowest defects, i.e. the distribution is lower since higher temperature values are more common in the histogram. The pattern for temperature distribution across smooth surface is affected by reflection while higher temperature distribution can be seen on rough surface. To allocate a suitable temperature range for post-processing of thermal image; all the readings were recorded at an ambient temperature

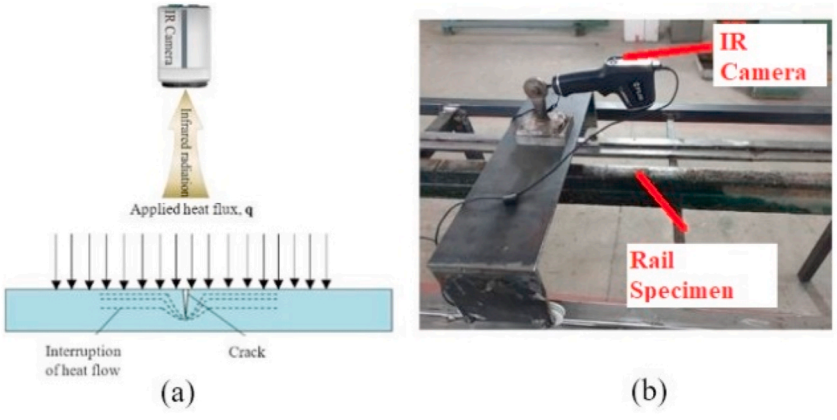

Fig. 7. Thermography inspection system configuration (a) Schematic for IRT (b) Experimental layout for IRT inspection system.

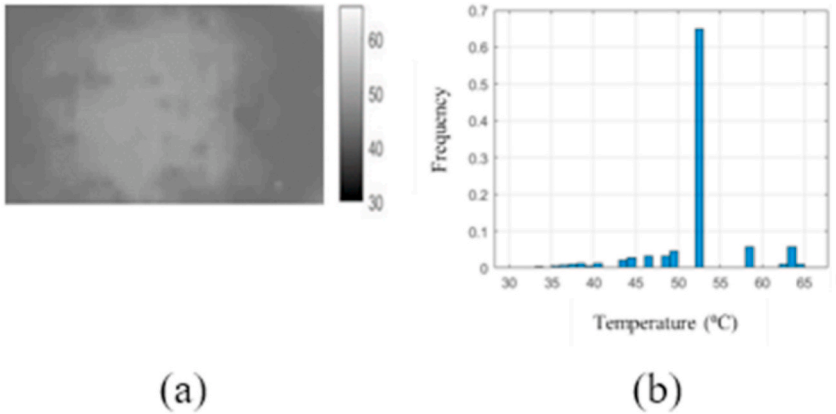

Fig. 8. Thermogram for non-defective surface (a) Post-processed IR image (b) Frequency of surface temperature distribution.

of 30 °C while maximum temperature was extrapolated based on direct relation of temperature and pixel intensity.

Quantitative characterization for each type of flaw can be made from frequency of temperature distribution. In Fig. 9 (a), (c), (e) and (g) transverse cracks are distinguishable in processed thermal images due difference in cooling rates between flaw and sound surface. This effect has also been depicted in histogram where average surface temperature has higher frequency than temperature distribution at surface imperfections. The same trend can also be observed for crack detection on smooth surface as shown in Fig. 9 (b), (d), (f) and (h) but temperature distribution in histogram is rather symmetrical as temperature gradient across the surface varies uniformly as compared to cracks on rough surface. Also, cooling rates is changing with depth of each crack resulting in a more vivid contrast between the shallower and deeper flaws.

SNR for transverse flaws has also been calculated using equation (10). For transverse flaws on smooth surface (TF1S to TF4S), the range of SNR is between 34 and 39 dB whereas for transverse flaws on rough surface (TF1R to TF4R) it lies between 32 and 37 dB. Nevertheless, thermal images in each scenario provides enhanced thermal contract for effective detection of surface flaws.

5. Conclusion

Infrared active thermography has been applied for characterization and detection of railroad surface flaws. Both longitudinal and transverse flaws were identified which is pivotal for reliability and safety with development of high-speed train networks. The results obtained provide a quantitative evaluation for railroad surface flaws on different type surface subjected to operation wear and harsh environmental conditions. To enhance the visual inspection of these flaws and reduce noise due to scattering of thermal radiation in surroundings; post-processing was applied to deduce a meaningful thermal contrast between defective and non-defective region. Further work is aimed to integrate artificial intelligence which would boost the robustness and overall efficiency of inspection system.

Authorship statement

Bilawal Ramzan: Conception and design of study, analysis and/or interpretation of data, Drafting the manuscript, Approval of the version of the manuscript to be published; **Muhammad Sohail Malik**: Conception and design of study, analysis and/or interpretation of data, revising the manuscript critically for important intellectual, Approval of the version of the manuscript to be published content; **Milena Martarelli**: revising the manuscript critically for important intellectual content, Approval of the version of the manuscript to be published; **Hafiz T Ali**: revising the manuscript critically for important intellectual content, Approval of the version of the manuscript to be published; **Mohammad Yusuf**: revising the manuscript critically for important intellectual content, Approval of the version of the manuscript to be published; **S.M. Ahmad**: revising the manuscript critically for important intellectual content (the names of all authors must be listed).

Declaration of competing interest

The authors declare that they have no known competing financial interests or personal relationships that could have appeared to influence the work reported in this paper.

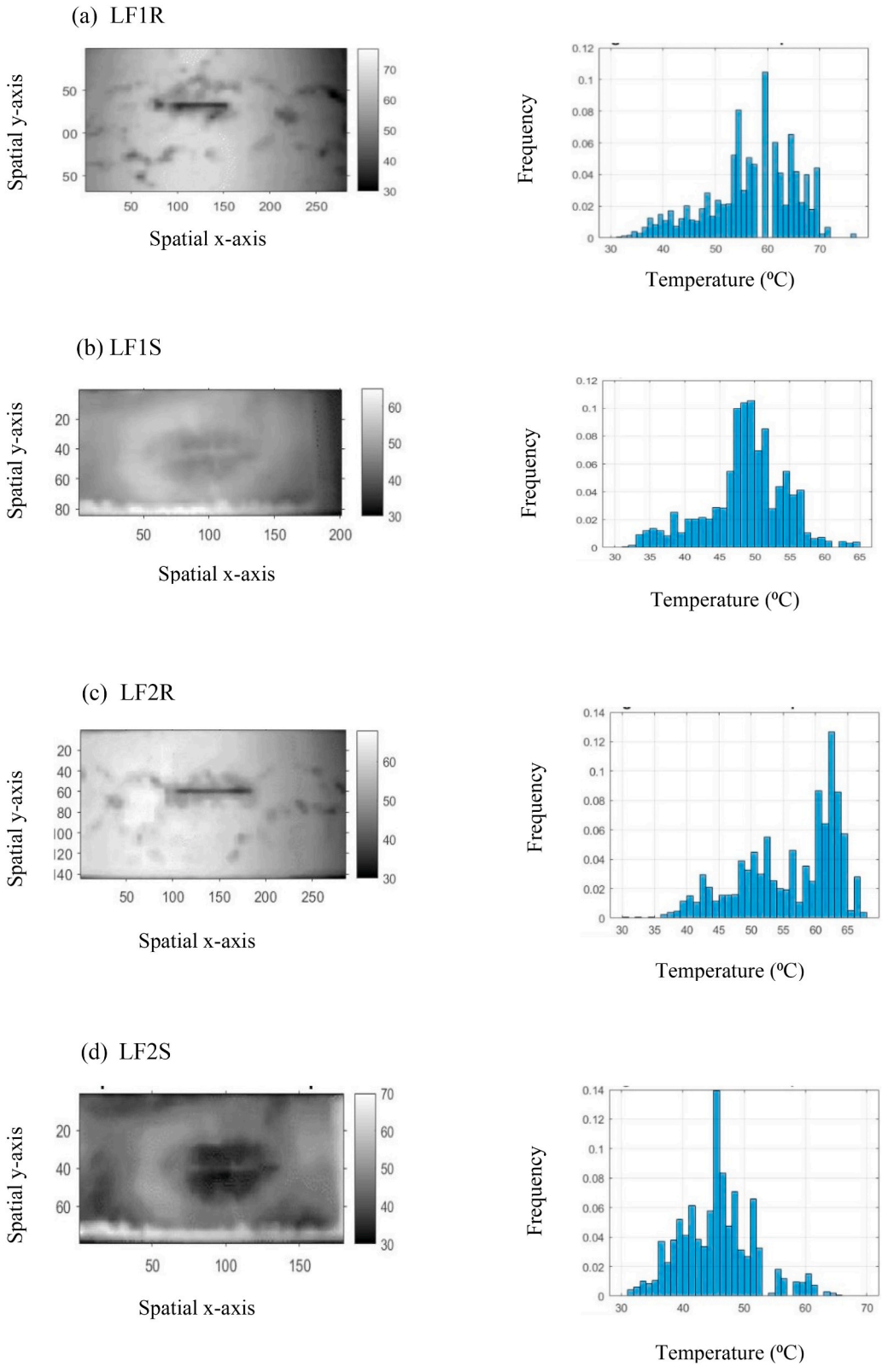

Fig. 9. Characterization of longitudinal flaws on rough and smooth surface.

(e) LF3R

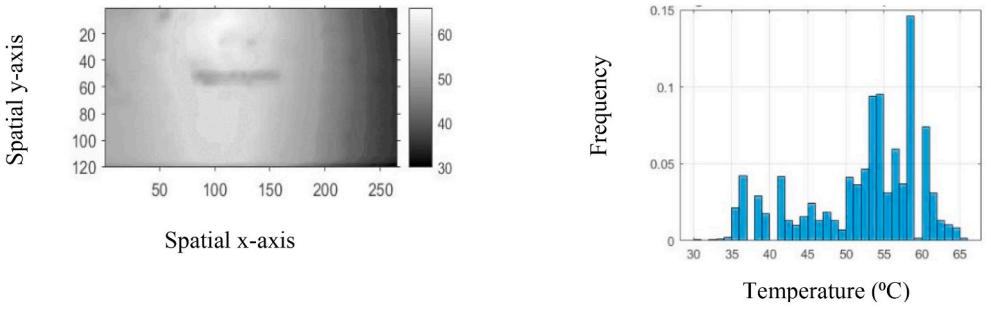

(f) LF3S

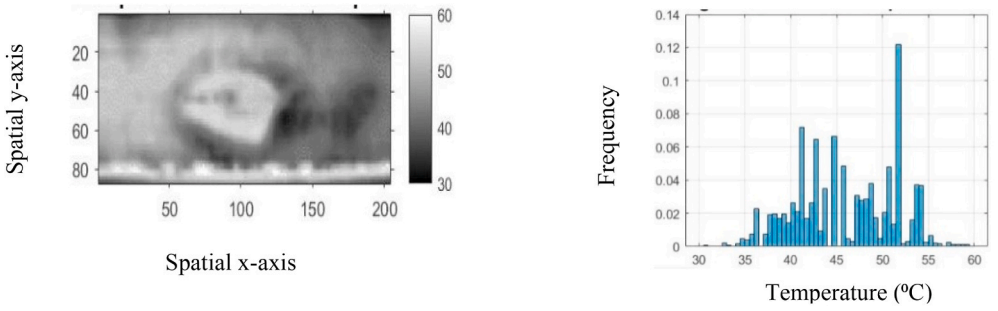

(g) LF4R

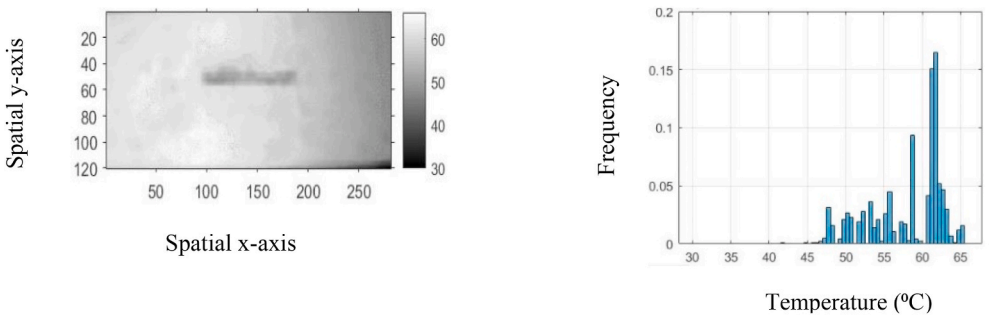

(h) LF4S

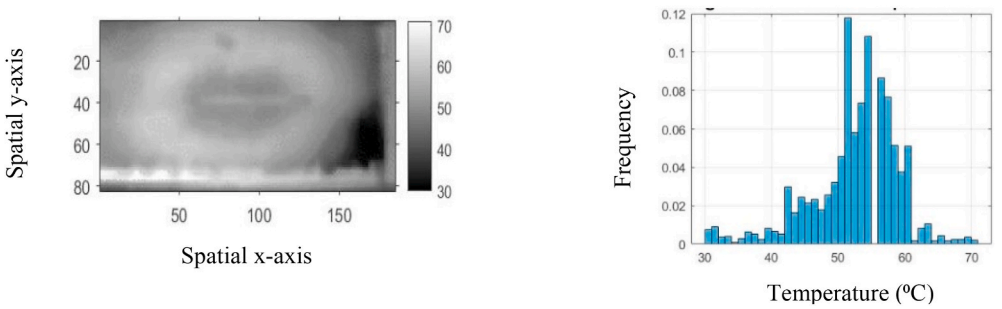

Fig. 9. (*continued*).

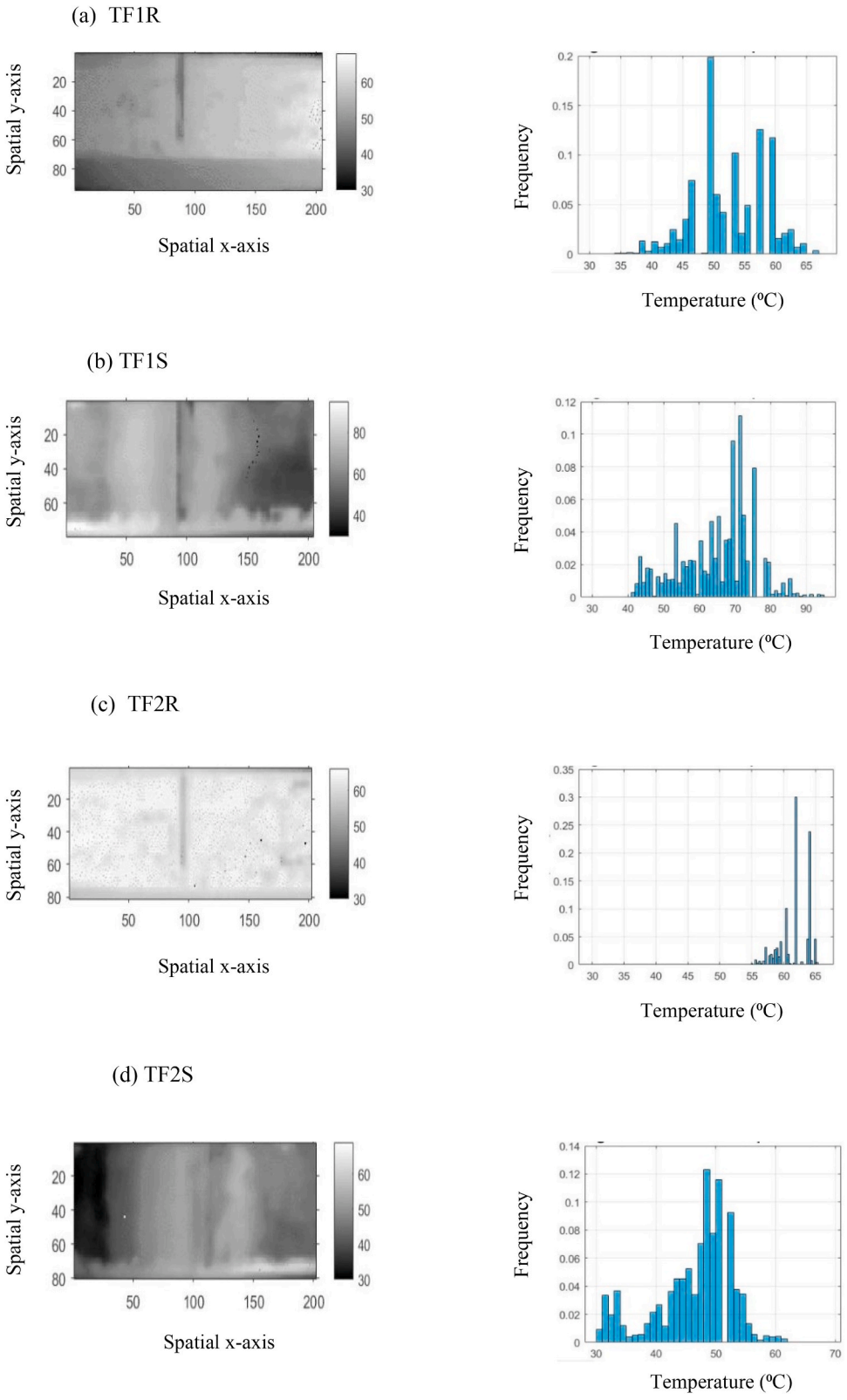

Fig. 10. Characterization of transverse flaws on rough and smooth surface.

(e) TF3R

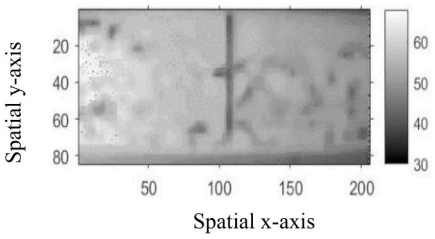

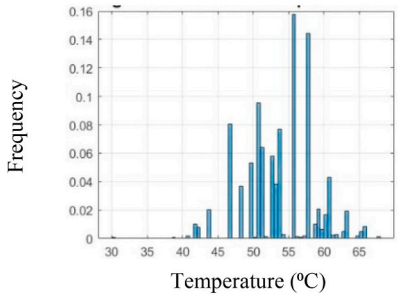

(f) TF3S

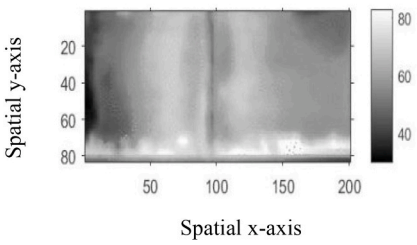

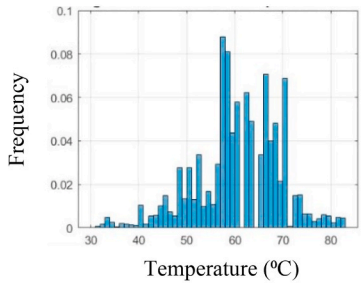

(g) TF4R

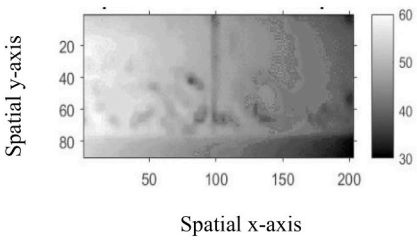

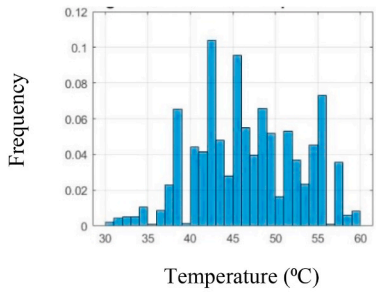

(h) TF4S

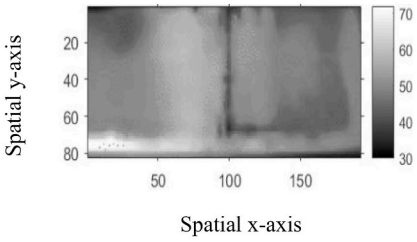

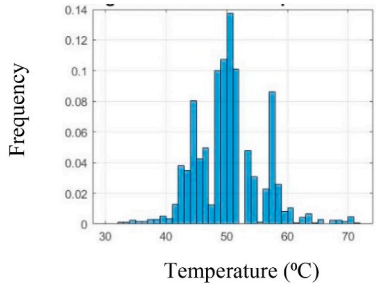

Fig. 10. (*continued*).

Acknowledgements

The current research is supported by Taif University Researchers Supporting Project number (TURSP-2020/293), Taif University, Taif, Saudi Arabia. Support from the Higher Education Commission of Pakistan under the program of NRPU is also acknowledged.

References

[1] Y.D. Li, C.B. Liu, N. Xu, X.F. Wu, W.M. Guo, J.B. Shi, A failure study of the railway rail serviced for heavy cargo trains, Case Stud. Eng. Fail. Anal. 1 (2013) 243–248, https://doi.org/10.1016/j.csefa.2013.09.003.
[2] A. Wilson, M. Kerr, Rail defects handbook, 1–83, http://extranet.artc.com.au/docs/eng/track-civil/guidelines/rail/RC2400.pdf, 2012.
[3] U. Zerbst, S. Beretta, Failure and damage tolerance aspects of railway components, Eng. Fail. Anal. 18 (2011) 534–542, https://doi.org/10.1016/j.engfailanal.2010.06.001.
[4] B. Peng, N. Zhang, Y.L. Gao, Static and dynamic analysis of railway reinforced system with cross-beams, Math. Probl Eng. 2014 (2014), https://doi.org/10.1155/2014/513606.
[5] R. Clark, Rail flaw detection: overview and needs for future developments, in: NDT E Int, Elsevier, 2004, pp. 111–118, https://doi.org/10.1016/j.ndteint.2003.06.002.
[6] J.L. Rose, C.M. Lee, T.R. Hay, Y. Cho, I.K. Park, RAIL INSPECTION WITH GUIDED WAVES, 2006.
[7] M. Raj, D. Mallik, S. Bansal, R.K. Saini, R.K. Ajmeria, Non-Destructive Testing and Inspection of Rails at JSPL-Ensuring Safety and Reliability, (n.d).
[8] R. Edwards, S. Dixon, X.J. Ultrasonics, undefined, Depth Gauging of Defects Using Low Frequency Wideband Rayleigh Waves, Elsevier, 2006 (n.d.), https://www.sciencedirect.com/science/article/pii/S0041624X05000831. (Accessed 27 August 2020).
[9] R. Edwards, S. Dixon, X.J.-N.& e International, undefined, Characterisation of Defects in the Railhead Using Ultrasonic Surface Waves, Elsevier, 2006 (n.d.), https://www.sciencedirect.com/science/article/pii/S0963869506000090. (Accessed 27 August 2020).
[10] K. Mcaughey, M. Potter, P.P.-18th W.C. on, undefined, Rail Track Condition Monitoring Using Electromagnetic Acoustic Transducers, Ndt.Net., 2012 (n.d.), https://www.ndt.net/article/wcndt2012/papers/649_wcndtabstract00650.pdf. (Accessed 27 August 2020).
[11] R. Edwards, C. Holmes, Y.F.-I.-N., undefined, Ultrasonic Detection of Surface-Breaking Railhead Defects, Ingentaconnect.Com., 2008 (n.d.), https://www.ingentaconnect.com/content/bindt/insight/2008/00000050/00000007/art00005. (Accessed 27 August 2020).
[12] P.L. Mazzeo, M. Nitti, E. Stella, N. Ancona, A. Distante, An automatic inspection system for the hexagonal headed bolts detection in railway maintenance, in: IEEE Conf. Intell. Transp. Syst. Proceedings, ITSC, 2004, pp. 417–422, https://doi.org/10.1109/itsc.2004.1398936.
[13] M. Bentley, F. Lund, A.W.-N.I. Limited, undefined NSP1001, undefined, Field Gradient Imaging Technology, Applications and Solutions for Component and Structural Integrity for Track and Rolling Stock for the Rail Industry, 2004 (n.d.).
[14] R. Shunmugam, K. Ramesh, Modeling and Detecting Damage in Rails & Avoidance of Collision in the Tracks 2 (2011) 1–16.
[15] A. Cavuto, M. Martarelli, G. Pandarese, G.M. Revel, E.P. Tomasini, Experimental investigation by Laser Ultrasonics for train wheelset flaw detection, in: J. Phys. Conf. Ser., Institute of Physics Publishing, 2018, 012015, https://doi.org/10.1088/1742-6596/1149/1/012015.
[16] A. Cavuto, M. Martarelli, G. Pandarese, G.M. Revel, E.P. Tomasini, Train wheel diagnostics by laser ultrasonics, Meas. J. Int. Meas. Confed. 80 (2016) 99–107, https://doi.org/10.1016/j.measurement.2015.11.014.
[17] K. Bruzelius, D. Mba, An initial investigation on the potential applicability of Acoustic Emission to rail track fault detection, NDT E Int. 37 (2004) 507–516, https://doi.org/10.1016/j.ndteint.2004.02.001.
[18] M.S. Malik, A. Cavuto, M. Martarelli, G. Pandarese, G.M. Revel, Reliability analysis of laser ultrasonics for train axle diagnostics based on model assisted POD curves, in: AIP Conf. Proc., American Institute of Physics Inc., 2014, pp. 396–404, https://doi.org/10.1063/1.4879608.
[19] M.S. Malik, Model assisted POD of laser-ultrasonics NDT for train axles: a review, in: Int. Conf. Electr. Electron. Optim. Tech. ICEEOT 2016, Institute of Electrical and Electronics Engineers Inc., 2016, pp. 4645–4648, https://doi.org/10.1109/ICEEOT.2016.7755600.
[20] C. Meola, Infrared thermography of masonry structures, Infrared Phys. Technol. 49 (2007) 228–233, https://doi.org/10.1016/j.infrared.2006.06.010.
[21] S. Stipetic, M. Kovacic, Z. Hanic, M. Vrazic, Measurement of excitation winding temperature on synchronous generator in rotation using infrared thermography, IEEE Trans. Ind. Electron. 59 (2012) 2288–2298, https://doi.org/10.1109/TIE.2011.2158047.
[22] J. Zhu, P.J. Withers, J. Wu, F. Liu, Q. Yi, Z. Wang, G.Y. Tian, Characterization of rolling contact fatigue cracks in rails by eddy current pulsed thermography, IEEE Trans. Ind. Informatics. 3203 (2020), https://doi.org/10.1109/tii.2020.3003335, 1–1.
[23] D.B. Durocher, D. Loucks, Infrared windows applied in switchgear assemblies: taking another look, IEEE Trans. Ind. Appl. 51 (2015) 4868–4873, https://doi.org/10.1109/TIA.2015.2456064.
[24] Y. Hu, W. Cao, J. Ma, S.J. Finney, D. Li, Identifying PV module mismatch faults by a thermography-based temperature distribution analysis, IEEE Trans. Device Mater. Reliab. 14 (2014) 951–960, https://doi.org/10.1109/TDMR.2014.2348195.
[25] M. Manana, A. Arroyo, A. Ortiz, C.J. Renedo, S. Perez, F. Delgado, Field winding fault diagnosis in DC motors during manufacturing using thermal monitoring, in: Appl. Therm. Eng., 2011, pp. 978–983, https://doi.org/10.1016/j.applthermaleng.2010.11.023.
[26] R. Alfredo Osornio-Rios, J.A. Antonino-Daviu, R. De Jesus Romero-Troncoso, Recent industrial applications of infrared thermography: a review, IEEE Trans. Ind. Informatics. 15 (2019) 615–625, https://doi.org/10.1109/TII.2018.2884738.
[27] S. Doshvarpassand, C. Wu, X.W.-I.P.& Technology, undefined, An Overview of Corrosion Defect Characterization Using Active Infrared Thermography, Elsevier, 2019 (n.d.), https://www.sciencedirect.com/science/article/pii/S1350449518307084. (Accessed 27 August 2020).
[28] L. Cheng, B. Gao, G.Y. Tian, W. Lok Woo, G. Berthiau, Impact damage detection and identification using eddy current pulsed thermography through integration of PCA and ICA, IEEE Sensor. J. 14 (2014) 1655, https://doi.org/10.1109/JSEN.2014.2301168.
[29] R. Yang, Y. He, Eddy current pulsed phase thermography considering volumetric induction heating for delamination evaluation in carbon fiber reinforced polymers, Appl. Phys. Lett. 106 (2015), https://doi.org/10.1063/1.4922524.
[30] X. Xiao, B. Gao, G. yun Tian, K. qing Wang, Fusion model of inductive thermography and ultrasound for nondestructive testing, Infrared Phys. Technol. 101 (2019) 162–170, https://doi.org/10.1016/j.infrared.2019.06.016.
[31] B. Gao, L. Bai, W.L. Woo, G. Tian, Thermography pattern analysis and separation Defect characterization by inductive heated thermography AIP Conf Integrated active transient thermography for rapid nondestructive analysis of sputtering target bond integrity, Cit. Appl. Phys. Lett. 104 (2014) 1100, https://doi.org/10.1063/1.4884644.
[32] J. Wilson, G. Tian, I. Mukriz, D. Almond, PEC thermography for imaging multiple cracks from rolling contact fatigue, NDT E Int. 44 (2011) 505–512, https://doi.org/10.1016/j.ndteint.2011.05.004.
[33] P. Jäckel, U. Netzelmann, The influence of external magnetic fields on crack contrast in magnetic steel detected by induction thermography, Quant. InfraRed Thermogr. J. 10 (2013) 237–247, https://doi.org/10.1080/17686733.2013.852414.
[34] B.B. Lahiri, S. Bagavathiappan, C. Soumya, V. Mahendran, V.P.M. Pillai, J. Philip, T. Jayakumar, Author's Personal Copy Infrared Thermography Based Defect Detection in Ferromagnetic Specimens Using a Low Frequency Alternating Magnetic Field, Elsevier, 2014, https://doi.org/10.1016/j.infrared.2014.02.004.
[35] U. Netzelmann, G. Walle, S. Lugin, A. Ehlen, S. Bessert, B. Valeske, Induction thermography: principle, applications and first steps towards standardisation, Quant. InfraRed Thermogr. J. 13 (2016) 170–181, https://doi.org/10.1080/17686733.2016.1145842.
[36] S.M. Shepard, in: A.E. Rozlosnik, R.B. Dinwiddie (Eds.), Advances in Pulsed Thermography, Quality, International Society for Optics and Photonics, 2001, pp. 511–515, https://doi.org/10.1117/12.421032.

[37] S. Lagüela, L. Díaz-Vilariño, D.R.-N.-D. Techniques, undefined 2016, Infrared Thermography: Fundamentals and Applications, Books.Google.Com (n.d.), https://books.google.com.pk/books?hl=en&lr=&id=4QfYCwAAQBAJ&oi=fnd&pg=PA113&dq=Infrared+thermography:+fundamentals+and+applications.+Non-Destructive+Tech+Eval+Struct+Infrastruct+2016:113. (Accessed 1 September 2020), –, 38&ots=DvDaki6Fbo&sig=_NPY57nn3CvlU-TfrmUZkCp3Q3I.
[38] (PDF) Neonatal Monitoring Technologies: Design for Integrated Solutions, Book chapter: neonatal infrared thermography imaging (n.d.), https://www.researchgate.net/publication/210290210_Neonatal_Monitoring_Technologies_Design_for_Integrated_Solutions_Book_chapter_Neonatal_Infrared_Thermography_Imaging. (Accessed 2 October 2020).
[39] R. Usamentiaga, P. Venegas, J. Guerediaga, L. Vega, J. Molleda, F. Bulnes, Infrared thermography for temperature measurement and non-destructive testing, Sensors 14 (2014) 12305–12348, https://doi.org/10.3390/s140712305.
[40] I. Garrido, S. Lagüela, P. Arias, Infrared thermography's application to infrastructure inspections, Infrastructure 3 (2018) 35, https://doi.org/10.3390/infrastructures3030035.
[41] W. Swiderski, Lock-in thermography to rapid evaluation of destruction area in composite materials used in military applications, in: Sixth Int. Conf. Qual. Control by Artif. Vis., SPIE, 2003, p. 506, https://doi.org/10.1117/12.515159.
[42] Z. Qu, P. Jiang, W. Zhang, Development and application of infrared thermography non-destructive testing techniques, Sensors 20 (2020) 1–27, https://doi.org/10.3390/s20143851.
[43] L. Dong, B. Wang, H. Wang, M. Xiang, X. Chen, G. Ma, Y. Di, W. Guo, J. Kang, X. Zhou, Effects of crack surface roughness on crack heat generation characteristics of ultrasonic infrared thermography, Infrared Phys. Technol. 106 (2020) 103262, https://doi.org/10.1016/j.infrared.2020.103262.
[44] D. Hahn, M. Özisik, Heat conduction. https://books.google.com/books?hl=en&lr=&id=C9qwb9Vymy8C&oi=fnd&pg=PR15&ots=KRnxpvay52&sig=7P6elAGlkbobyZwyorqA7aqpe1g, 2012. (Accessed 1 September 2020).
[45] Z. Andleeb, S. Malik, G. Hussain, H. Khawaja, J. Roemer, G. Boiger, M. Moatamedi, Multiphysics study of infrared thermography (IRT) applications, Int. J. Multiphys. 14 (2020) 249–271, https://doi.org/10.21152/1750-9548.14.3.249.
[46] W. -Web, Rail Sections HT-Height BW-Width of Base HW-Width of Head FD-Fishing BD-Depth of Base E-Bolt Hole Elevation, (n.d).
[47] M. Zhu, G. Xu, J.H. Zhou, R.M. Wang, X.L. Gan, Study on service performance of 880 MPa-grade and 980 MPa-grade rail steels, IOP Conf. Ser. Mater. Sci. Eng. 244 (2017), 012025, https://doi.org/10.1088/1757-899x/244/1/012025.
[48] Bhn, Heavy Haul Tracks Specification Grade Chemical Composition Mechanical Properties % by Mass Rm (MPa) Elongation, 2017.
[49] G.L. Nicholson, A.G. Kostryzhev, X.J. Hao, C.L. Davis, Modelling and experimental measurements of idealised and light-moderate RCF cracks in rails using an ACFM sensor, NDT E Int. 44 (2011) 427–437, https://doi.org/10.1016/j.ndteint.2011.04.003.
[50] O. Trushkevych, R.S. Edwards, Characterisation of small defects using miniaturised EMAT system, NDT E Int. 107 (2019) 102140, https://doi.org/10.1016/j.ndteint.2019.102140.
[51] A. Colantonio, M. Theauvette, Thermographic Assessment Specification Requirements for Commissioning and Building Condition Applications, (n.d).
[52] B. Ramzan, S. Malik, S.M. Ahmad, M. Martarelli, Railroads surface crack detection using active thermography, in: 2021 Int. Bhurban Conf. Appl. Sci. Technol., IEEE, 2021, pp. 183–197, https://doi.org/10.1109/IBCAST51254.2021.9393210.
[53] R. Usamentiaga, C. Ibarra-Castanedo, X. Maldague, More than fifty shades of grey: quantitative characterization of defects and interpretation using SNR and CNR, J. Nondestr. Eval. 37 (2018), https://doi.org/10.1007/s10921-018-0479-z.